Boston University

OpenBU **http://open.bu.edu**

BU Open Access Articles BU Open Access Articles

2023-06-01

Predicting the yield of small transiting exoplanets around mid-M and ultracool dwarfs in the Na...

This work was made openly accessible by BU Faculty. Please share how this access benefits you. Your story matters.

Version	Published version
Citation (published version):	P. Tamburo, P.S. Muirhead, C.D. Dressing. 2023. "Predicting the Yield of Small Transiting Exoplanets around Mid-M and Ultracool Dwarfs in the Nancy Grace Roman Space Telescope Galactic Bulge Time Domain Survey" The Astronomical Journal, Volume 165, Issue 6, pp.251-251. https://doi.org/10.3847/1538-3881/acd1de

https://hdl.handle.net/2144/46837

Boston University

Boston University Libraries
OpenBU

The Astronomical Journal, 165:251 (13pp), 2023 June https://doi.org/10.3847/1538-3881/acd1de
© 2023. The Author(s). Published by the American Astronomical Society.
OPEN ACCESS

Predicting the Yield of Small Transiting Exoplanets around Mid-M and Ultracool Dwarfs in the Nancy Grace Roman Space Telescope Galactic Bulge Time Domain Survey

Patrick Tamburo[1], Philip S. Muirhead[1], and Courtney D. Dressing[2]
[1] Department of Astronomy & The Institute for Astrophysical Research, Boston University, 725 Commonwealth Ave., Boston, MA 02215, USA; tamburop@bu.edu
[2] Department of Astronomy, 501 Campbell Hall, University of California at Berkeley, Berkeley, CA 94720, USA
Received 2023 March 17; revised 2023 April 26; accepted 2023 May 1; published 2023 May 25

Abstract

We simulate the yield of small (0.5–4.0 $R_\oplus$) transiting exoplanets around single mid-M and ultracool dwarfs (UCDs) in the Nancy Grace Roman Space Telescope Galactic Bulge Time Domain Survey. We consider multiple approaches for simulating M3–T9 sources within the survey fields, including scaling local space densities and using Galactic stellar population synthesis models. These approaches independently predict ∼100,000 single mid-M dwarfs and UCDs brighter than a Roman F146 magnitude of 21 that are within the survey fields. Assuming planet occurrence statistics previously measured for early-to-mid-M dwarfs, we predict that the survey will discover 1347^{+208}_{-124} small transiting planets around these sources, each to a significance of 7.1σ or greater. Significant departures from this prediction would test whether the occurrence rates of small planets increase or decrease around mid-M dwarfs and UCDs compared to early-M dwarfs. We predict the detection of 13^{+4}_{-3} habitable, terrestrial planets ($R_p < 1.23\,R_\oplus$) in the survey. However, atmospheric characterization of these planets will be challenging with current or near-future space telescope facilities due to the faintness of the host stars. Nevertheless, accurate statistics for the occurrence of small planets around mid-M dwarfs and UCDs will enable direct tests of predictions from planet formation theories and will determine our understanding of planet demographics around the objects at the bottom of the main sequence. This understanding is critical given the prevalence of such objects in our galaxy, whose planets may therefore comprise the bulk of the galactic census of exoplanets.

Unified Astronomy Thesaurus concepts: Exoplanet astronomy (486); Transit photometry (1709); Astronomical simulations (1857); Extrasolar rocky planets (511); Surveys (1671); L dwarfs (894); Brown dwarfs (185); M dwarf stars (982); Late-type dwarf stars (906); T dwarfs (1679)

1. Introduction

The NASA Kepler mission (Borucki et al. 2010) revealed a significant anticorrelation between stellar host mass and the occurrence rates of short-period, small exoplanets ($P \lesssim 200$ days, $R_p \leqslant 4.0\,R_\oplus$; Howard et al. 2012; Mulders et al. 2015). Early-M dwarfs were found to host short-period super-Earths ($1.0\,R_\oplus < R_p < 2.8\,R_\oplus$) at a rate roughly three times higher than that of F dwarfs in the Kepler field (Mulders et al. 2015), and possess around 2.5 short-period planets with $R_p \leqslant 4.0\ R_\oplus$ per star, on average (Dressing & Charbonneau 2013, 2015; Gaidos et al. 2016). This anticorrelation has also been observed in radial velocity (RV) surveys (Sabotta et al. 2021; Pinamonti et al. 2022).

Naively, the anticorrelation between host mass and short-period small planet occurrence rates is surprising, since lower-mass stars have, on average, less-massive reservoirs of dust in their protoplanetary disks with which to form planets through core accretion (Andrews et al. 2013; Pascucci et al. 2016). Factors beyond disk mass alone must be at play to explain the observed trends. One possibility is that giant planets, which occur more frequently around higher-mass hosts (e.g., Johnson et al. 2010), limit the flux of planet-forming pebbles to the inner disk and hence preferentially suppress the formation of short-period super-Earths around higher-mass stars. Mulders et al. (2021) found that that this pebble-flux-limiting scenario can explain observed Kepler planet occurrence rates and predicted an overturn in short-period, super-Earth planet occurrence rates at host masses below $\sim 0.5\,M_\odot$, with essentially no super-Earths formed at an orbital distance of 0.3 au around hosts with masses below $0.1\,M_\odot$.

However, there are currently few observational constraints on small planet occurrence rates around hosts with masses below $0.3\,M_\odot$ (SpT ∼ M3), owing to their intrinsic faintness and spectral energy distributions that peak in the near-infrared (NIR). Hardegree-Ullman et al. (2019) used Kepler detections to measure the occurrence rates of planets on 0.5–10 day orbits with radii between 0.5 and 2.5 $R_\oplus$ around mid-type M dwarfs (M3–M5) and reported a tentative increase from $0.86^{+1.32}_{-0.68}$ to $3.07^{+5.49}_{-2.49}$ planets per star over those spectral types; however, their small sample size of 13 planets around seven stars lead to occurrence rates with large fractional uncertainties. Their results are supported by occurrence rates measured with RV detections from the CARMENES survey, which found a significant increase in the occurrence rate of low-mass ($1\,M_\oplus < M_p \sin i < 10\,M_\oplus$) planets with periods less than 10 days around stars with $M_\star < 0.34\,M_\odot$ compared to higher-mass stars (Sabotta et al. 2021). However, recent results from the Transiting Exoplanet Survey Satellite (TESS; Ricker et al. 2015) suggest that the mission's yield of 0.5–2.0 $R_\oplus$ planet candidates around nearby mid-M dwarfs is best produced by a constant or decreasing planet occurrence rate compared to early-M dwarfs (Brady & Bean 2022; Ment & Charbonneau 2023).

Occurrence rates of small planets around ultracool dwarfs (UCDs, spectral types M7 and later; Kirkpatrick et al. 1997) are

Original content from this work may be used under the terms of the Creative Commons Attribution 4.0 licence. Any further distribution of this work must maintain attribution to the author(s) and the title of the work, journal citation and DOI.

even less constrained. To date, only one system of small exoplanets has been confirmed transiting a UCD host: the seven Earth-sized planets around TRAPPIST-1 (Gillon et al. 2016, 2017). Data from the full TRAPPIST-Ultra-Cool Dwarf Transit Survey (Gillon et al. 2013) were used to place a lower limit of 10% on the occurrence rates of TRAPPIST-1b-like planets around their sample of 40 UCDs (Lienhard et al. 2020). Other data sets have been used to place upper limits on planet occurrence rates around UCDs. He et al. (2017) used Spitzer observations of 44 brown dwarfs and found that for periods less than 1.28 days, the occurrence rate of planets with radii between 0.75 and 3.25 $R_\oplus$ is less than $67\% \pm 1\%$. Sagear et al. (2020) and Sestovic & Demory (2020) both used K2 data to search for transiting planets around UCDs, but were not able to constrain the occurrence rates of small exoplanets strongly due to low signal-to-noise ratio (S/N) data, owing to the operation at visible wavelengths. Dedicated ground-based transit surveys at NIR wavelengths like the Search for habitable Planets EClipsing ULtra-cOOl Stars (SPECULOOS; Delrez et al. 2018; Murray et al. 2020; Sebastian et al. 2021), the ExoEarth Discovery and Exploration Network (EDEN; Gibbs et al. 2020), and the Perkins INfrared Exosatellite Survey (PINES; Tamburo et al. 2022a) are actively searching for small planets around UCDs, but they would have to detect hundreds of planets to determine occurrence rates to a similar precision as measured for early-M dwarfs with Kepler.

The Nancy Grace Roman Space Telescope,[3] currently slated for launch in 2026, is the next flagship mission of the NASA Astrophysics Division (Spergel et al. 2015; Akeson et al. 2019). It is a 2.4 m telescope that will be stationed at the second Sun–Earth Lagrange point (L2), and it will be equipped with two instruments: (1) the Coronagraph Instrument (CGI; Noecker et al. 2016; Mennesson et al. 2020), a technology demonstration instrument that will perform optical imaging, polarimetry, and spectroscopy of circumstellar disks and exoplanets, and (2) the Wide Field Instrument (WFI; Domber et al. 2019, 2022), an NIR camera for imaging and slitless spectroscopy which will be used to perform the mission's three "Core Community Surveys," these being the High Latitude Time Domain Survey, the High Latitude Wide Area Survey, and the Galactic Bulge Time Domain Survey.[4] WFI will use a mosaic of 18 H4RG detectors to capture images with more than 200 times the field of view of the NIR channel of Hubble's WFC3 instrument, but with similar image quality (Akeson et al. 2019; Domber et al. 2022).

The design of the Galactic Bulge Time Domain Survey (hereafter "the survey") was motivated by the detection of microlensing planets (see, e.g., Spergel et al. 2015; Penny et al. 2019; Johnson et al. 2020). The microlensing technique probes a different parameter space than the transit method, being most sensitive to detecting planets at $\gtrsim$1 au from the host star. For typical microlensing events in the Galactic bulge, for example, the method is most sensitive to planets at a distance of $\sim$[2–4] au $(M/M_\odot)^{1/2}$ (Gaudi 2012; Penny et al. 2019). A large-scale microlensing survey would, therefore, complement the known population of close-in planets from transit surveys like Kepler and TESS, as well as the populations discovered by the RV and direct imaging methods. To maximize the number of microlensing detections, the survey will perform time series photometry of seven fields that make up a $\sim$2 deg^2 region of the Galactic bulge, using NIR filters to reduce the effect of dust extinction in the Galactic plane. These seven fields will be targeted in six, 72 day seasons over the course of a nominal five-year primary mission, with photometry performed using an F146 filter (0.93–2.00 μm) and an F087 filter (0.76–0.98 μm). The survey will primarily be executed in the F146 filter, with one 46.8 s F146 exposure obtained in each of the seven fields every 909.6 s. The secondary F087 filter will be used to obtain color information about the sources, with one 286 s F087 exposure taken every 12 hr. We refer readers to Penny et al. (2019) for an in-depth summary of the current "Cycle 7" design of the survey, but note that its exact implementation (e.g., number of fields, cadence, filters, etc.) is still being refined.

Spergel et al. (2015) estimated that the survey will provide photometry with a precision of 1% or better for around 20 million dwarf stars. The large number of target stars, high photometric precision, and the 15 minute cadence will allow the survey to double as a search for transiting exoplanets; the NIR wavelength coverage makes it particularly well suited to search for transiting planets around mid-M dwarfs and UCDs. Montet et al. (2017) simulated the transiting planet yield of the survey, estimating that more than 100,000 could be detected around FGKM stars, including several thousand around M dwarfs, specifically. However, they only considered planets as small as 2 $R_\oplus$, which neglects the sizable population of 0.5–2.0 $R_\oplus$ planets that have been detected around early-M dwarf stars (Dressing & Charbonneau 2015; Gaidos et al. 2016). They also did not consider the detection of planets around L- and T-type dwarfs, spectral types that may host an abundance of short-period planets (e.g., Limbach et al. 2021; Tamburo et al. 2022b). Recent work by Limbach et al. (2023) on the proposed Transiting Exosatellites, Moons, and Planets in Orion (TEMPO) Survey has explored the possibility of applying Roman Guest Observer time series observations to detecting planets around low-mass stars, brown dwarfs, and free-floating planets in the Orion Nebular Cluster (ONC). They estimate that a 30 day survey of the ONC could detect 14 transiting satellites around free-floating planets and 54 transiting satellites around brown dwarfs, demonstrating the power of the observatory for detecting transiting companions around hosts at the bottom of the main sequence and beyond.

In this paper, we present a simulation of the transiting planet yield around mid-M spectral types and later in the Core Community Survey, specifically, and investigate the survey's potential for extending measurements of planet occurrence rates into the ultracool regime. The paper is organized as follows. In Section 2, we describe the creation of a synthetic sample of mid-M dwarfs and UCDs in the Roman microlensing fields using measured space densities from nearby volume-complete samples, which is compared against results from Galactic stellar population synthesis models. It also details the time series photometry that was simulated for these targets and which was injected with a population of transiting planets. Section 3 describes the recovery of these planets, and Section 4 discusses the potential implications of these discoveries.

2. Host Simulation

2.1. Simulated Photometry

The expected noise performance of the WFI drives the magnitude and distance limits that we apply in our simulations. The time domain survey will primarily use an F146 filter. This

[3] Formerly the Wide Field Infrared Survey Telescope (WFIRST).
[4] https://roman.gsfc.nasa.gov/observations.html

Table 1
Parameters Describing the Expected Noise Performance of Roman's WFI and the Format of the Survey

Parameter	Value	Units
Dark current	1.072	e^- s^{-1} pix^{-1}
Read noise	12.12	e^- rms
Sky background	3.43	e^- s^{-1} pix^{-1}
Aperture size	9	pix
F146 zero-point	2.078e-10	erg s^{-1} cm^{-2} $Å^{-1}$
Noise floor	1	mmag
Exposure time	46.8	s
Cadence	909.6	s
Season length	72	days
Number of seasons	6	⋯

Note. Values follow the Cycle 7 survey design detailed in Penny et al. (2019). The F146 zero-point was sourced from the Spanish Virtual Observatory Filter Profile Service.

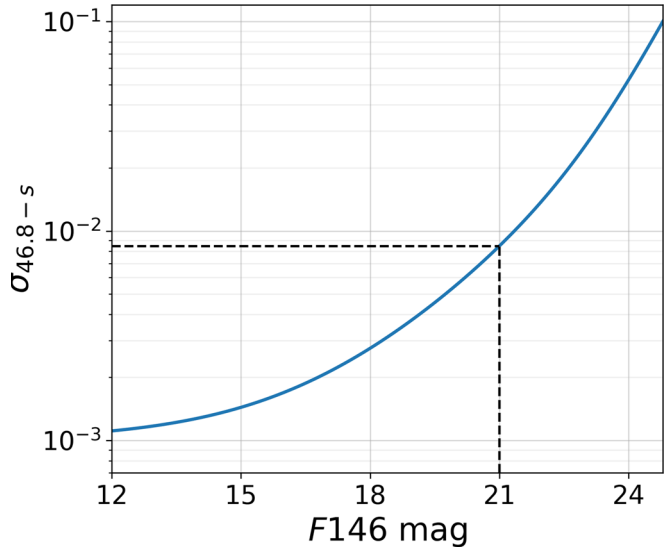

Figure 1. The standard deviation of normalized photometry in a single 46.8 s exposure in the F146 band, modeled using the parameters listed in Table 1. The F146 = 21 magnitude cutoff and its corresponding ∼1% single-exposure standard deviation are indicated in dashed black lines.

filter will provide wavelength coverage from 0.93–2.00 μm, entirely encompassing the standard Y , J, and H photometric passbands (e.g., Bessell 2005). We modeled the standard deviation of normalized photometry in the F146 filter using the properties listed in Table 1, the values of which were sourced from the WFIRST Cycle 7 design described in Penny et al. (2019). The model assumes a sky background count rate that was determined using a time-dependent zodiacal light model evaluated at the midpoint of the survey seasons. It also assumes a nine-pixel aperture (which was found to produce the best photometry in the crowded microlensing fields in Penny et al. 2019) and a constant systematic noise floor of 1 mmag. The assumed noise floor becomes the dominant noise component for magnitudes less than F146 ≈ 16.8, and its effect can be seen in the gradual tapering off of the curve in Figure 1 for the brightest source magnitudes. This assumption has little impact on the total planet yield of our simulations, since very few detections are made around sources brighter than F146 = 16.8 (see Section 4.1).

The resulting noise model for a 46.8 s exposure as a function of F146 magnitude is shown in Figure 1. A per-exposure uncertainty of 1% is achieved around a magnitude of 21 in the F146 band, and we use this as the magnitude cutoff for sources throughout the remainder of this study. We note that this is the same magnitude cutoff used in Montet et al. (2017). For the earliest spectral types considered in this study (M3), the magnitude cutoff corresponds to a maximum distance of about 3.5 kpc. See Table 2 for estimates of the maximum distances of mid-M dwarfs and UCDs with F146 < 21 in different effective temperature ($T_{\rm eff}$) bins.

Data time stamps in the F146 band were generated assuming a 909.6 s cadence over six, 72 day seasons. These six seasons were assumed to take place in two campaigns, with three seasons near the start of the mission and three seasons near the end (Spergel et al. 2015). The three seasons in each campaign were separated by half a year. Every 12 hr, we removed a simulated exposure in the F146 band to replicate expected interruptions caused by photometry in the time domain survey's secondary F087 bandpass (Penny et al. 2019). While we included these interruptions, we did not simulate photometry in the F087 band because the 12 hr cadence in this filter is unlikely to sample many in-transit points for the average ∼1 hr transit durations around mid-M and UCD spectral types. For example, a planet on a 7.2 day period (near the median detected orbital period in our simulations, see Section 4.1) with a 1 hr transit duration would be sampled by a maximum of just ∼5 in-transit exposures in the F087 band over the 432 day survey, compared to ∼200 in-transit exposures in the F146 band.

In the absence of constraints on spacecraft/detector systematics, we simulated target photometry at these time stamps using purely uncorrelated Gaussian ("white") noise based on the noise model shown in Figure 1. However, we note

Table 2
Local Space Densities of Single M3–T9 Dwarfs Used in the Simulation Described in Section 2.2

$T_{\rm eff}$ (K)	SpT	Density (pc^{-3})	$d_{\rm max}$ (pc)
3300–3150	M3.0–M4.0	0.0072 ± 0.0007	3500
3150–3000	M4.0–M5.0	0.0051 ± 0.0006	2500
3000–2850	M5.0–M6.0	0.0029 ± 0.0005	1850
2850–2700	M6.0–M7.0	0.0024 ± 0.0004	1420
2700–2550	M7.0–M8.0	0.0018 ± 0.0004	1210
2550–2400	M8.0–M9.0	0.0013 ± 0.0003	1070
2400–2250	M9.0–L0.0	0.0008 ± 0.0002	840
2250–2100	L0.0–L1.0	⩾0.0003	680
2100–1950	L1.0–L2.0	0.0006 ± 0.0001	620
1950–1800	L2.0–L3.0	0.0004 ± 0.0001	550
1800–1650	L3.0–L4.5	0.0005 ± 0.0001	380
1650–1500	L4.5–L6.0	0.0004 ± 0.0001	320
1500–1350	L6.0–L8.0	0.0007 ± 0.0001	270
1350–1200	L8.0–T1.5	0.0015 ± 0.0002	250
1200–1050	T1.5–T5.0	0.0008 ± 0.0002	190
1050–900	T5.0–T6.5	0.0012 ± 0.0002	130
900–750	T6.5–T7.5	0.0016 ± 0.0002	110
750–600	T7.5–T8.5	0.0021 ± 0.0003	80
600–450	T8.5–T9.0	0.0021 ± 0.0003	40

Note. Spectral types corresponding to these temperature ranges were estimated using the M dwarf $T_{\rm eff}$ scale from Rajpurohit et al. (2013) for temperatures above 2800 K and the field M6–T9 $T_{\rm eff}$ scale from Faherty et al. (2016) for temperatures below 2800 K. We also list $d_{\rm max}$, an estimate of the maximum distance of objects within each $T_{\rm eff}$ range with F146 < 21.

that systematic "red" noise would necessarily impose a higher detection threshold to achieve the same number of statistical false positives as expected for the uncorrelated noise case considered here (e.g., Pont et al. 2006), which would in turn decrease our yield estimates.

2.2. Simulated Host Population Using Local Space Densities

The population of mid-M dwarfs and UCDs with F146 < 21 in the survey fields is not currently known. The faintest such sources have Gaia magnitudes of ∼26, which is well beyond the detection limits of that survey, especially in the crowded Galactic plane (e.g., Gaia Collaboration et al. 2016; Hodgkin et al. 2021). They also lie beyond the detection limits of previous NIR imaging campaigns with the Two Micron All Sky Survey (2MASS; Skrutskie et al. 2006), the Spitzer Space Telescope (Churchwell et al. 2009), the Wide-Field Infrared Survey Explorer (WISE; Wright et al. 2010), the Panoramic Survey Telescope and Rapid Response System (Pan-STARRS1; Chambers et al. 2016), and the DECam Plane Survey (DECaPS; Schlafly et al. 2018).

In this section, we describe a simulation that we performed to estimate the number of mid-M dwarf and UCD sources in the survey fields with F146 < 21 by using measured space densities from volume-complete samples in the solar neighborhood. In particular, we used the 15 pc sample of mid-M dwarfs from Winters et al. (2021; hereafter W21) and the 20 pc sample of L, T, and Y dwarfs from Kirkpatrick et al. (2021; hereafter K21). We elected to use only the sources in these samples that are presumed to be single objects, excluding sources in multiple systems. We did this because multiple systems, even though they may be resolved in the local samples, are unlikely to be resolved at the distances under consideration in this work (out to 3.5 kpc), and unresolved multiple systems complicate the interpretation of any detected transiting planet signals (e.g., Bouma et al. 2018). Out of the 512 M dwarfs with 0.1–0.3 $M_\odot$ in the 15 pc sample from W21, 290 are presumed to be single; out of the 525 L, T, and Y dwarfs in the 20 pc sample from K21, 438 are presumed to be single.

The W21 sample reports mass measurements for their sources, while the K21 sample reports source $T_{\rm eff}$. For the purposes of our simulation, we wish to employ the space densities of mid-M dwarfs and UCDs in terms of one of these variables, and we chose to use $T_{\rm eff}$. We converted the 290 mass measurements of single M dwarfs from W21 to estimates of $T_{\rm eff}$ using the 10 Gyr isochrone from Baraffe et al. (2015). We then counted the number of sources in the W21 sample in 150 K-wide $T_{\rm eff}$ bins, enforcing an upper $T_{\rm eff}$ limit of 3300 K (∼M3) and a lower limit of 2850 K (∼M6). We assumed Poisson errors on these counts, and converted the counts to space densities using the 15 pc sample volume.

The W21 and K21 measurements do not provide space densities for ∼M6–M9.5 dwarfs. Rather than exclude these types from the simulation, we filled in the gap by assuming a linear transition between the two sets of densities.[5] This approach qualitatively reproduces the sharp decrease in source counts over the M7–M9.5 spectral range seen in a magnitude-limited sample of 34,000, such targets in Ahmed & Warren (2019). The resulting space densities used in this study are given in Table 2 and visualized in Figure 2. The W21 densities are shown in blue, the K21 densities are shown in red, and the assumed densities of M6–M9.5 dwarfs are shown in orange. The space densities are highest around M3–M6 spectral types, reflecting the peak of the stellar initial mass function (IMF) near 0.2–0.3 $M_\odot$ (e.g., Kroupa 2002; Chabrier 2003; Bastian et al. 2010). The densities then shallow out and show a rise at the latest spectral types, reflecting the fact that as substellar objects age, they progressively cool and pile up in the lowest temperature bins.

The densities were measured over volumes near the Sun and do not reflect the exponential increase in star counts in the Milky Way's thin and thick disks in the direction of the Galactic center. This exponential increase is commonly modeled as a function of radial distance d with scale length $\ell_{\rm d}$ and vertical distance above the Galactic plane z with scale height z_d (e.g., McMillan 2017). Since the survey is performed near the Galactic midplane (see Figure 3), we ignore any scaling effects due to z. However, we do scale the local space densities of our simulated sources with d using the following relations:

$$n_t(d) = n_0 \exp\left(\frac{d}{\ell_t}\right), \quad (1)$$

$$n_T(d) = f_p n_0 \exp\left(\frac{d}{\ell_T}\right). \quad (2)$$

Here, n_0 is the local space density of mid-M dwarfs and UCDs given in Table 2, $\ell_{\rm t}$ is the radial scale length of the thin disk, f_p is the local density normalization of the thick disk to the thin disk, and ℓ_T is the radial scale length of the thick disk. Accurate determinations of $\ell_{\rm t}$ and ℓ_T are notoriously difficult, as their measurement must contend with source confusion and dust extinction in the Galactic plane. A review of 130 papers on the subject by Bland-Hawthorn & Gerhard (2016) revealed a range of 1.8–6.0 kpc, for example. Measurements of f_p are also difficult because it is degenerate with the scale heights of both the thin and thick disks (e.g., Reylé & Robin 2001). We decided to account for this uncertainty in our simulations by drawing $\ell_{\rm t}$, ℓ_T, and f_p from Gaussian distributions $N(\mu, \sigma)$, with central value μ and standard deviation σ given by the recommendations from Bland-Hawthorn & Gerhard (2016). Each iteration, we drew $\ell_{\rm t}$ from $N(2500, 400)$ pc, ℓ_T from $N(2000, 200)$ pc, and f_p from $N(0.04, 0.02)$, where we required $f_p > 0$.

We implemented our source simulation as follows. We first divided the 3.5 kpc simulation volume up into 25 pc spherical shells[6]. In each shell, we set the space densities for sources in the temperature bins by drawing from Gaussian distributions with means and standard deviations given by the values and uncertainties reported in Table 2. This was not done for the bin without an uncertainty, which was conservatively assigned its reported lower limit each loop. We scaled these densities with the distance to the front of the shell d using Equations (1) and (2) to simulate populations for the thin and thick disks respectively.

We then simulated source counts in the temperature bins within each shell by multiplying the space densities of the shell in question by the shell's volume. We multiplied these counts

[5] The assumption of a different form for the transition (e.g., an exponential decrease) would not strongly impact our results, as M6–M9.5 dwarfs make up only ∼5% of all sources in our simulations with F146 < 21 (see Figure 5).

[6] We tested the simulation with finer resolution shells and found that they did not significantly alter our results.

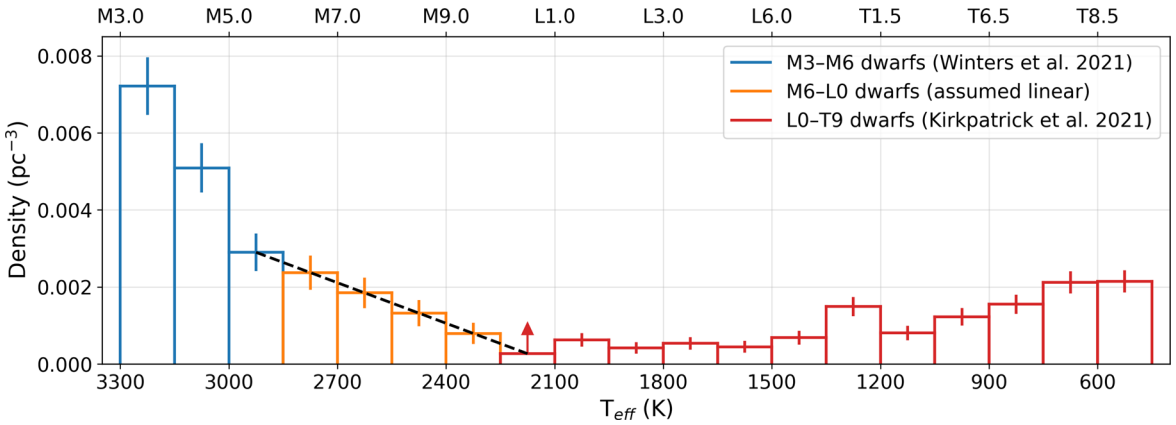

Figure 2. Local space densities of single M3–T9 dwarfs as a function of effective temperature used in the simulation described in Section 2.2. The top axis is given as a function of spectral type, the values of which were determined using the M dwarf temperature scale of Rajpurohit et al. (2013) for temperatures above 2800 K and the temperature scale for field M6–T9 dwarfs of Faherty et al. (2016) for temperatures below 2800 K. W21 densities are shown in blue and have been converted from a mass scale to a temperature scale using the 10 Gyr isochrone of Baraffe et al. (2015). K21 densities are shown in red. The densities of M6–M9.5 dwarfs are indicated in orange and were assumed to connect the W21 and K21 densities linearly. The linear fit that was used to generate these estimates is shown as a black dashed line. Error bars indicate the 1σ uncertainty on each bin, which were taken to be Poissonian. The 2100–2250 K bin is a lower limit and is indicated with an upward arrow.

by the fractional area of the Roman time domain survey on the sky (1.96 deg^2/41253 deg^2) to approximate the number of sources expected within the survey footprint. We randomly positioned the resulting number of expected sources in each temperature bin across the 126 detector positions that make up the survey footprint (18 detectors at seven field pointings; see Figure 3), assigning them random temperatures within the appropriate temperature bin and random distances within the bounds of the shell in question. Each target was also assigned a random age using a uniform distribution from 0.1–10 Gyr.

We then assigned each target a mass M and a radius R given the $T_{\rm eff}$ and age values using evolutionary models. If a source had a $T_{\rm eff} > 2250$ K, we used the low-mass star evolutionary models of Baraffe et al. (2015), whereas if the source had a $T_{\rm eff} < 2250$ K, we used the Sonora Bobcat brown dwarf evolutionary models from Marley et al. (2021). We first identified the four model points that most closely bracketed the target's $T_{\rm eff}$ and age values. We then performed a linear 2D interpolation of the mass and radius values belonging to these four entries and used the resulting functions to evaluate the expected M and R for the given $T_{\rm eff}$ and age values. We used the M and R values to calculate the log of the surface gravity ($\log g$) in cm s^{-2}.

Next, we calculated the magnitude of each source in a number of different photometric bands using BT-Settl models (Allard et al. 2012) covering the temperature range of 500–3300 K (in steps of 100 K) and using $\log(g)$ values of 4.5, 5.0, and 5.5. We assumed solar metallicity for each source. We assigned each source the closest matching model based on its $T_{\rm eff}$ and $\log g$ values, scaled the model fluxes to the flux received at Earth by multiplying by a factor of $(R/d)^2$, and multiplied by the light collecting area of the telescope, assuming a primary diameter of 2.36 m and an obscured fraction of 13.9% (Penny et al. 2019). We used publicly available filter bandpasses to calculate magnitudes in the Pan-STARRS r, i, and z bands, 2MASS J band, and Roman F146 band.[7]

[7] Pan-STARRS filters were obtained from http://svo2.cab.inta-csic.es/svo/theory/fps3/index.php?mode=browse&gname=PAN-STARRS&asttype=. 2MASS filter curves were obtained from http://svo2.cab.inta-csic.es/theory/fps/index.php?id=2MASS/. Roman filters were obtained from https://roman.gsfc.nasa.gov/science/WFI_technical.html.

Finally, we applied an extinction value to the magnitude in each band using the latest version of the Bayestar dust map (Green et al. 2015, 2018, 2019), accessed through the Python package `dustmaps` (Green 2018). This map provides probabilistic 3D reddening estimates based on parallax measurements from Gaia DR2 and stellar colors from Pan-STARRS1 and 2MASS photometry, which can be converted to extinction estimates in various filters. We used these conversion factors to translate the reddening value returned for the 3D coordinates of each source to extinction in the r, i, z, J, and F146 bands. We approximated the conversion factor in the F146 band by averaging the conversion factors in the 2MASS J, H, and K_S bands.

We repeated this simulation 1000 times to sample sufficiently the range of source counts that result from randomly sampling the W21 and K21 space densities, ℓ_t, ℓ_T, and f_p, from Gaussian distributions within each shell. In Figure 4, we show distribution of counts of mid-M dwarf and UCD sources with F146 < 21, which has a mean of $75{,}500^{+11{,}800}_{-7000}$ sources.

We show the distributions of the average values of various parameters for all sources across the 1000 instances of our simulation in Figure 5. This figure shows magnitudes in the F146, r, i, z, and J bands, along with the distances, effective temperatures, spectral types, masses, and radii. The central value and 1σ range is indicated for each of these distributions. The 99.9% percentiles on the r, i, z, and J magnitudes of our sources are 27.5, 24.9, 23.3, and 21.4, respectively. Imaging with sensitivity to these magnitude limits (or comparable limits in other red/optical and NIR bands) will thus be required to identify the ~75,500 mid-M dwarf and UCD sources that we expect with F146 < 21 within the Roman fields. This prospect may be realized with the upcoming Vera C. Rubin Observatory, which will provide seeing-limited imagery of the survey fields with 5σ point-source depths that will approach or surpass the required magnitude limits over the course of the anticipated 10 yr survey operation (Ivezić et al. 2019), or with the Roman survey data themselves.

Figure 5 shows that the targets in our simulated sample are located at an average distance of 1963^{+543}_{-667} pc. They have masses of $0.18^{+0.03}_{-0.04}$ $M_\odot$, radii of $0.20^{+0.02}_{-0.04}$ $R_\odot$, and spectral types of M4 plus or minus one subtype, on average. We expect relatively few L and T dwarfs in the Roman fields with

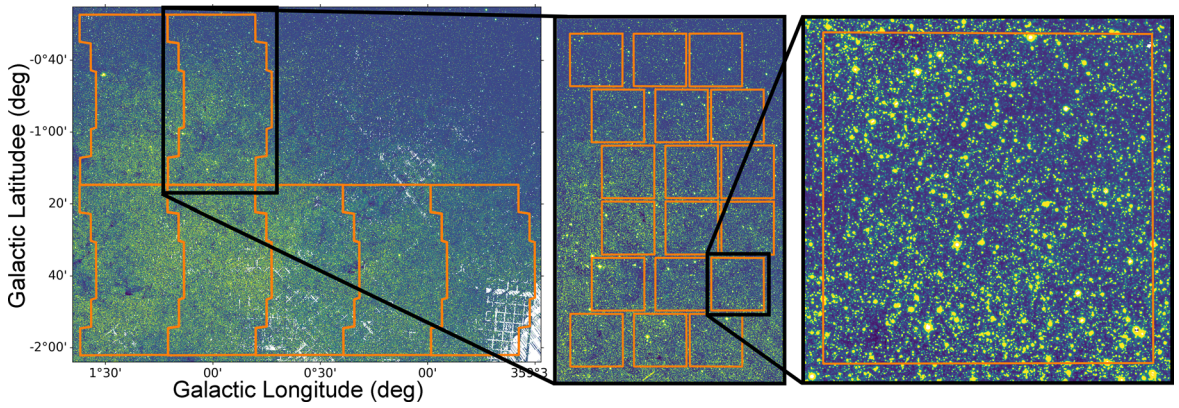

Figure 3. The on-sky footprint of the Roman survey with archival z-band imagery from Pan-STARRS1 (Chambers et al. 2016). Bad pixels in the Pan-STARRS1 data are colored in white and are used to flag saturated sources, areas without survey coverage, etc. Left: the full survey footprint, covering $\sim$2 deg^2 of the Galactic bulge over seven fields. Field outlines are shown in orange. Middle: a single field, with outlines of the 18 detector pointings shown in orange. Right: one detector within this field. Field pointings were taken from Penny et al. (2019; https://github.com/mtpenny/wfirst-ml-figures).

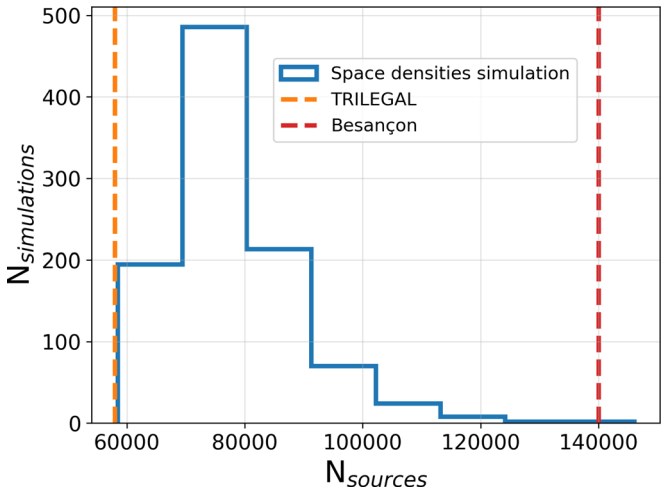

Figure 4. The distribution of the total number of single mid-M and UCD sources with F146 $<$ 21 in the survey fields over 1000 iterations of our simulation, with the scaled space densities shown in blue. This simulation predicts an average of $75{,}500^{+11{,}800}_{-7000}$ single mid-M dwarf and UCD sources in the survey fields (1σ range). Predictions from the Galactic stellar population synthesis models `TRILEGAL` and `Besançon` are marked with orange and red vertical lines, respectively (see Section 2.3 for more details).

F146 $<$ 21, finding just 57 such sources in each simulation, on average. This is because early-to-mid-L dwarfs have the lowest local space densities of any object considered in our simulation (see Figure 2), and the small radii and low temperatures of objects in the L and T spectral classes generally place them beyond our F146 = 21 cutoff.

2.2.1. Note on Metallicity Effects

The average metallicity of stars in the thin disk increases interior to the Sun's orbit. The furthest sources under consideration in this study, at a distance of 3.5 kpc toward the Galactic center, should be slightly enhanced in metals on average, with [Fe/H] $\approx$0.3 (e.g., Andrievsky et al. 2002; Pedicelli et al. 2009; Genovali et al. 2014). We did not account for the metallicity gradient in our modeling, but we do not expect that its inclusion would significantly impact our results. For a fixed NIR luminosity (e.g., M_K), the assumed metallicity has a negligible effect on the estimated radius and mass of an M dwarf (Delfosse et al. 2000; Bonfils et al. 2005; Mann et al. 2015, 2019), so including metallicity does not strongly impact the S/Ns of the transit events in our simulated data. Additionally, while there is an observed correlation between host metallicity and the occurrence rate of giant planets around various spectral types (Santos et al. 2004; Fischer & Valenti 2005; Johnson et al. 2010), such planets are rarely observed to transit around M-type stars (Dressing & Charbonneau 2013, 2015; Gaidos et al. 2016). While Anderson et al. (2021) found evidence of higher occurrence rates for "compact multiple" rocky planet systems around metal-poor K and M dwarfs compared to higher-metallicity stars, previous studies found no metallicity dependence for small planet occurrence rates around these spectral types (e.g., Mann et al. 2013; Gaidos et al. 2016). We therefore also ignore the potential effects that enhanced metallicity may have on small planet occurrence rates.

2.3. Simulated Host Population from Galactic Stellar Population Synthesis Models

In this section, we compare the simulated counts of mid-M dwarfs and UCDs from Section 2.2 to predictions from publicly available Galactic stellar population synthesis. Population synthesis models impose IMFs, star formation rates, and stellar evolutionary models to simulate populations of stars in different Galactic components, namely the thin disk, thick disk, halo, and bulge. This is a fundamentally different approach to our method of scaling local volume-complete samples of mid-M dwarfs and UCDs, and can act as an independent check on our predictions. We used the `TRILEGAL`[8] (Girardi et al. 2005) and `Besançon`[9] (Robin et al. 2003, 2012; Czekaj et al. 2014) models to make these comparisons.

We performed a `TRILEGAL` simulation in the direction of the center of survey fields ($\ell = 1\overset{\circ}{.}0$, $b = -0\overset{\circ}{.}667$) with a Roman F146 magnitude limit of 21. We performed this simulation over a field area of 0.1 deg^2 due to server limitations on the maximum computing time. We assumed the Sun's distance to the Galactic center to be 8000 pc. We used the model's default exponential dust extinction law and Chabrier (2001) log-normal IMF with binaries turned off. We used an exponential

[8] http://stev.oapd.inaf.it/cgi-bin/trilegal
[9] https://model.obs-besancon.fr/

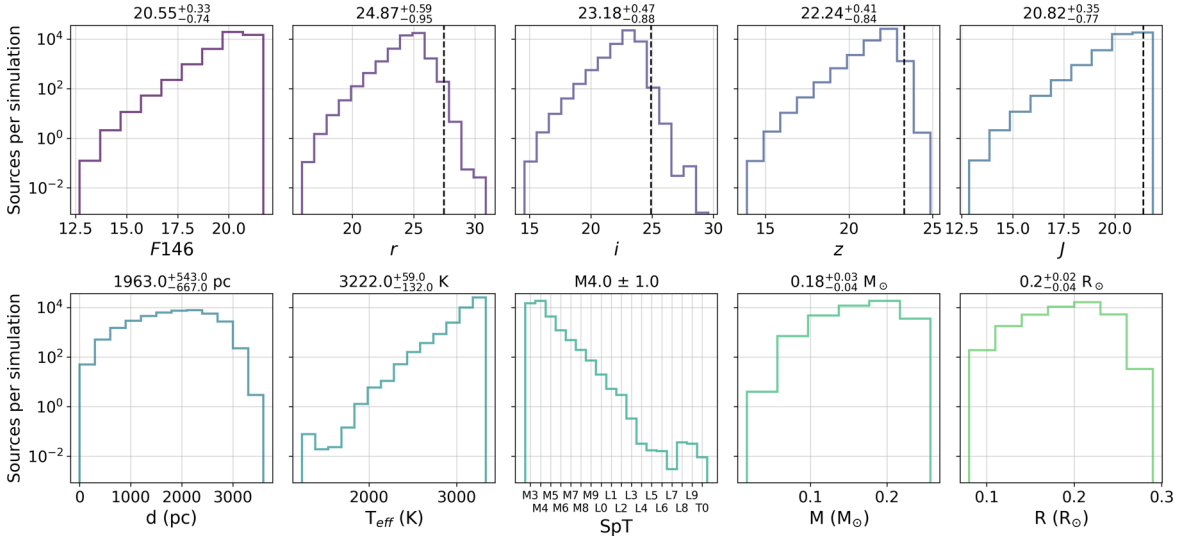

Figure 5. Distributions of host properties. The histograms are shown on a log scale and have been normalized to show the average counts in a single simulation. The 15.9%, 50%, and 84.1% percentiles of each distribution (i.e., the 1σ range) are reported at the top of each panel. Top row: source magnitudes in the F146, *r*, *i*, *z*, and *J* bands. Magnitudes were calculated using BT-Settl model spectra and were reduced by realistic dust extinction values. The 99.9% percentiles for the *r*, *i*, *z*, and *J* magnitudes (used in the Besançon simulation described in Section 2.3) are indicated by dashed black lines. Bottom row: distance in parsecs, effective temperature in Kelvin, spectral type, mass in solar masses, and radius in solar radii.

thin disk with a radial scale length of 2500 pc and a thick disk with a scale length of 2000 pc (i.e., the central values that were used to simulate the radial scale lengths in Section 2.2). We did not model the halo or bulge populations. This simulation produced 2956 single sources with $T_{\rm eff} < 3300$ K over the 0.1 deg^2 field area, which equates to about 58,000 sources over the full 1.96 deg^2 Roman survey area. This prediction is lower than the average number of sources produced in our simulation in Section 2.2 by about a factor of 1.3, and it is indicated as a vertical orange line in Figure 4.

`Besançon` does not currently support the Roman photometric system. Instead, we performed a simulation with magnitude limits based on the 99.9% percentiles on the *r*-, *i*-, *z*-, and *J*-band magnitudes described in Section 2.2. We performed this simulation centered on ($\ell = 1\overset{\circ}{.}0$, $b = -0\overset{\circ}{.}667$) over a field area of 1.96 deg^2. The simulation only supports source modeling out to spectral type M9, but such sources dominate the counts of objects with F146 < 21 in our simulation, so the exclusion of later types will not strongly affect the comparison with our results.

The `Besançon` results includes binary systems, with the binary probability as a function of source mass *M* (in solar masses) given by the following equation from Arenou (2011):

$$f(M) = 0.8388 \tanh 0.688M + 0.079 \quad (3)$$

.To approximate the number of single mid-M dwarfs and UCDs, we evaluated this equation for each source with $T_{\rm eff} < 3300$ K, removing it from the list if a number drawn from a random uniform distribution was less than the binary probability determined by its mass. Doing this, we found a total of 140,000 sources with $T_{\rm eff} < 3300$ K in the `Besançon` simulation, which is a factor of 1.9 times higher than the average predicted by our scaled space densities simulation. This prediction is indicated as a red line in Figure 4.

Thus, we find that the average number of mid-M dwarf and UCD sources in the Roman survey fields with F146 < 21 from our scaled space density simulation lies between the predictions from `TRILEGAL` and `Bensaçon`. Furthermore, all three predictions lie within a factor of three of each other. In the remainder of this work, we use the source samples that were created using the scaled space densities in Section 2.2, as they are intermediate between the predictions from the Galactic stellar population synthesis models. However, we note that if the population of mid-M dwarfs and UCDs in the Roman survey actually resembles the `TRILEGAL` prediction, our average planet yield estimates would be lower by a factor of about 1.3, whereas if it matches the `Besançon` prediction, our yield estimates would be enhanced by a factor of about 1.9.

3. Planet Injection and Recovery Simulation

3.1. Simulated Planet Population

We simulated planetary systems around each of the 1000 samples of mid-M dwarfs and UCDs created with our scaled space density simulation in Section 2.2. Planets were simulated using the results of Dressing & Charbonneau (2015; hereafter DC15), who used Kepler discoveries to measure planet occurrence rates around early-M dwarfs over a grid of planet radii (0.5–4.0 $R_\oplus$) and orbital periods (0.5–200 days). These are the nearest spectral types to the ones under consideration in this study with detailed planet occurrence rates. Significant deviations from the number of expected detections under the assumption of the DC15 occurrence rates will test for significant changes in the planet populations of mid-M dwarf and UCD sources (see Section 4.3).

For each simulated source, we first applied a random on-sky inclination, drawing from a $\sin i$ distribution. We then looped over the DC15 occurrence rate grid, simulating an orbiting planet with a random radius and period within the cell bounds if a randomly chosen number from a uniform distribution was less than the measured occurrence rate in the given cell. In multiplanet systems, we assumed that all planets were coplanar. We tested the resulting planetary system for orbital stability following the approach of Fabrycky et al. (2014), assuming circular orbits for all planets. For each pair of adjacent planets,

we calculated the mutual Hill radius, given by:

$$R_H = \left[\frac{M_{\rm in} + M_{\rm out}}{3M_h}\right]^{1/3} \frac{a_{\rm in} + a_{\rm out}}{2}, \quad (4)$$

where "in" indicates the inner planet, "out" indicates the outer planet, M is the planet mass, a is the planet semimajor axis, and M_h is the host mass. The planet masses were estimated using the mass–radius relation from `Forecaster` (Chen & Kipping 2017). While a variety of exoplanet mass–radius relationships exist in the literature (e.g., Weiss et al. 2013; Wolfgang et al. 2016; Bashi et al. 2017; Ning et al. 2018; Ulmer-Moll et al. 2019; Unterborn et al. 2023), the Hill radius is weakly dependent on planetary mass, so adopting a different model would likely not alter our stability analysis significantly. If the orbital separation of a pair of planets in units of their mutual Hill radii, $\Delta = (a_{\rm in} - a_{\rm out})/R_H$, is greater than a critical separation of $2\sqrt{3}$, the pair is considered to be stable. We also enforced the conservative heuristic of Fabrycky et al. (2014) for systems with more than three planets, which requires that adjacent inner and outer pairs of planets have a total separation greater than 18 in units of their mutual Hill radii, that is $\Delta_{\rm in} + \Delta_{\rm out} > 18$. We repeated the planet injection procedure for each source until these stability criteria were satisfied. The distribution of planets per star created with this procedure is approximately Poissonian with a mean of 2.4, consistent with the mean of 2.5 ± 0.2 planets per star measured for early-M dwarfs in DC15.

We then created light-curve models for each planet in the system using `BATMAN` (Kreidberg 2015), assuming a quadratic limb darkening law with coefficients interpolated from the tables of Claret & Bloemen (2011). Any planets that were found to transit (including grazing transits) were injected into their host's light curve. In multiplanet systems, each planet was injected individually, ignoring effects from simultaneous transit events. On average, 2656^{+502}_{-266} transiting planets were created each simulation.

3.2. Planet Recovery

Searching for planets with established transit search algorithms like box least squares (Kovács et al. 2002) or Transit Least Squares (Hippke & Heller 2019) would be computationally expensive for an average of 75,500 sources each with 40,000-point light curves across 1000 simulations. Computation time could be sped up by applying these search algorithms to binned data, but the 15 minutes cadence of the survey data means that only a handful of points can be averaged together before injected transits are shallowed out significantly. As a result, we adopted the approach of Montet et al. (2017), and phase-folded the planet-injected light curves on the known orbital period, considering a planet detected if its transit S/N exceeded a value of 7.1. The choice of this significance threshold is motivated by a desire to compare our results with the number of planets around mid-M and UCD spectral types in the Kepler and TESS missions, which used the same threshold. It also permits a direct comparison to the results of Montet et al. (2017).

However, the 7.1σ threshold was selected for the Kepler and TESS missions in an attempt to limit the number of statistical false positive transit detections over the course of the surveys to approximately one. It may not be appropriate for the Roman survey, which will search for transit events around a much larger number of stars (~200,000,000 versus ~100,000 in the Kepler survey; Spergel et al. 2015). We illustrate this with a simple example in Figure 6, which shows the theoretical single-search false alarm rate as a function of detection threshold for the Kepler mission from Jenkins et al. (2002). If we assume that the number of independent statistical tests conducted in searching for transits in a single Roman light curve is roughly equal to the number required for a single Kepler light curve, we can use the theoretical curve to estimate the detection threshold where the false alarm rate equals 1/200,000,000, which it does at 8.1σ. While a full investigation into the appropriate detection threshold for the Roman survey is beyond the scope of this work, this example illustrates that a higher detection threshold higher than 7.1σ may be required to limit the number of statistical false positive detections to one.

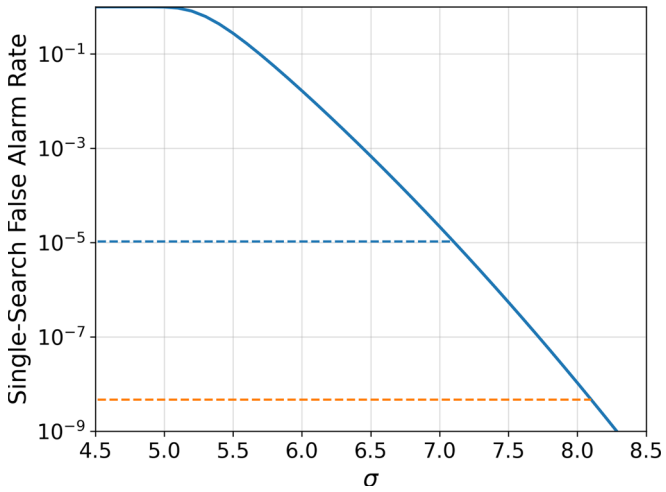

Figure 6. The theoretical single-search false alarm rate as a function of detection threshold for the Kepler mission from Jenkins et al. (2002; solid blue line). A dashed blue line indicates the desired false positive rate of 1/100,000 for Kepler, which is achieved at a detection threshold of 7.1σ. A dashed orange line shows an estimate for the Roman survey, where a false positive rate of 1/200,000,000 is achieved at a detection threshold of 8.1σ.

We adopt the following definition of transit S/N:

$$S/N = \frac{\phi_{\rm oot} - \phi_{\rm it}}{\sqrt{\sigma_{\rm oot}^2 + \sigma_{\rm it}^2}}, \quad (5)$$

where $\phi_{\rm oot}$ is the mean out-of-transit flux, $\phi_{\rm it}$ is the mean in-transit flux, $\sigma_{\rm oot}$ is the standard deviation of the out-of-transit flux, and $\sigma_{\rm it}$ is the standard deviation of the in-transit flux. All of these quantities are evaluated using unbinned data that have been phased on the known orbital period.

An example planet recovery in our simulation is shown in Figure 7. It shows simulated Roman time domain survey photometry of an M5 planet host with F146 = 16.5, $R_h = 0.133\,R_\odot$, $M_h = 0.108\,M_\odot$, $T_{\rm eff} = 2895$ K, a distance of 193 pc, and an age of 2.68 Gyr.[10] A planet was injected into this light curve with a radius of 1.24 $R_\oplus$, an orbital period of 27.0 days, $a/R_h = 136$, and $i = 89.^\circ9$. This planet was recovered to an S/N of 40 using Equation (5) evaluated on the unbinned phased data.

[10] We use the subscript "h" to denote parameters of the planet hosts in our simulation, instead of the traditional "s" for "star." This is because the sources in our simulation include brown dwarfs.

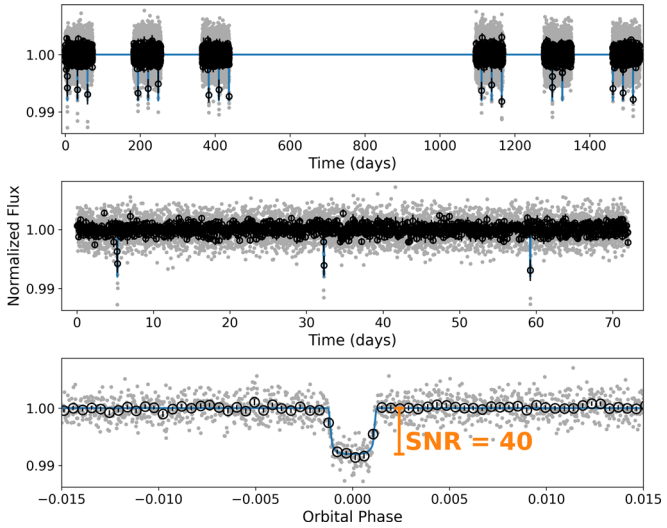

Figure 7. An example detection of a planet in our injection and recovery simulation. The host is an M5 dwarf with F146 = 16.5, $R_h = 0.133\ R_\odot$, $M_h = 0.108\ M_\odot$, $T_{\rm eff} = 2895$ K, a distance of 193 pc, and an age of 2.68 Gyr. The planet has a radius of 1.24 $R_\oplus$, an orbital period of 27.0 days, a/R_h= 136, and $i = 89.^\circ9$. Top: the full simulated light curve, which consists of six, 72 day campaigns, three near the start of the mission and three near the end. Gray points show the 46.8 s photometry evaluated at a 909.6 s cadence, and black points with error bars show the photometry binned over 1.5 hr timescales. The transit model is shown in blue. Middle: the first of the six campaigns. Bottom: the phase-folded data which we use to assess the transit significance. Black points with error bars show the phased photometry binned over 20 points. The transit was recovered in the phased photometry to an S/N of 40 using Equation (5).

4. Results

4.1. Total Transiting Planet Yield

We injected planets into our 1000 samples of mid-M dwarfs and UCD targets. An average of 1347^{+208}_{-124} planets were detected in each simulation under the assumption of the DC15 planet occurrence rates. Hosts were frequently found to host 2+ transiting planets, with with an average of 274^{+41}_{-30} multiple systems identified per simulation. Of the detected multiple systems, 78% were found to be two-planet systems, 18% to be three-planet systems, and 3% to be four-planet systems. Systems with five or more of planets were rare, contributing to fewer than half a percent of the total yield of planets detected in multiple systems, combined. The highest number of planets identified in one system across all our simulations was six.

We break down the average total number of planets as a function of $T_{\rm eff}$ in Table 3. These results are compared against the confirmed and candidate planets with $R_p < 4\ R_\oplus$ around hosts with $T_{\rm eff} < 3300$ K detected by the Kepler (including K2) and TESS missions, which were tabulated using data from the NASA Exoplanet Archive[11] on 2022 October 27. We visualize these results in Figure 8, which shows the planet detections from a representative iteration of our simulation compared to the detections from Kepler and TESS.

Our results suggest that the Roman survey will provide more than an order of magnitude increase in the number of known small planets around hosts with $T_{\rm eff} < 3300$ K. For example, 77 confirmed or candidate planets with $R_p < 4\ R_\oplus$ have been identified in Kepler or TESS data around hosts with 2700 K $< T_{\rm eff} <$ 3300 K (SpT ∼M3–M7); we predict that Roman will enable the detection of 1334^{+209}_{-123} such planets. While the number of detections are biased toward the earliest spectral types under consideration in this study, we expect that Roman will

[11] https://exoplanetarchive.ipac.caltech.edu/

Table 3
Planets Detected in Our Injection and Recovery Simulation as a Function of $T_{\rm eff}$/SpT under the Assumption of the DC15 Occurrence Rates

$T_{\rm eff}$ (K)	SpT	Roman	Kepler	TESS
3300–3150	M3.0–M4.0	488^{+114}_{-80}	8	18
3150–3000	M4.0–M5.0	631^{+104}_{-92}	10	21
3000–2850	M5.0–M6.0	163^{+33}_{-27}	5	11
2850–2700	M6.0–M7.0	47 ± 11	0	4
2700–2550	M7.0–M8.0	18^{+7}_{-6}	0	0
2550–2400	M8.0–M9.0	7 ± 4	0	0
2400–2250	M9.0–L0.0	2^{+3}_{-1}	0	0
2250–450	L0.0–T9.0	1^{+1}_{-1}	0	0

Note. The 15.9%, 50%, and 84.1% percentiles are reported for the number of detected planets in our simulations. Few planets were detected on average around L- and T-type dwarfs, so the total detections around these types are presented as a single range. The table also shows confirmed and candidate detections of planets smaller than 4 $R_\oplus$ around these spectral types from the Kepler and TESS missions. The reported Kepler detections include confirmed and candidate planets from both the Kepler and K2 missions, excluding candidates that were flagged as false positives. The reported TESS detections include confirmed planets and TESS objects of interest that have not been classified as false positives. The tables detailing these detections were accessed from the NASA Exoplanet Archive on 2022 October 27.

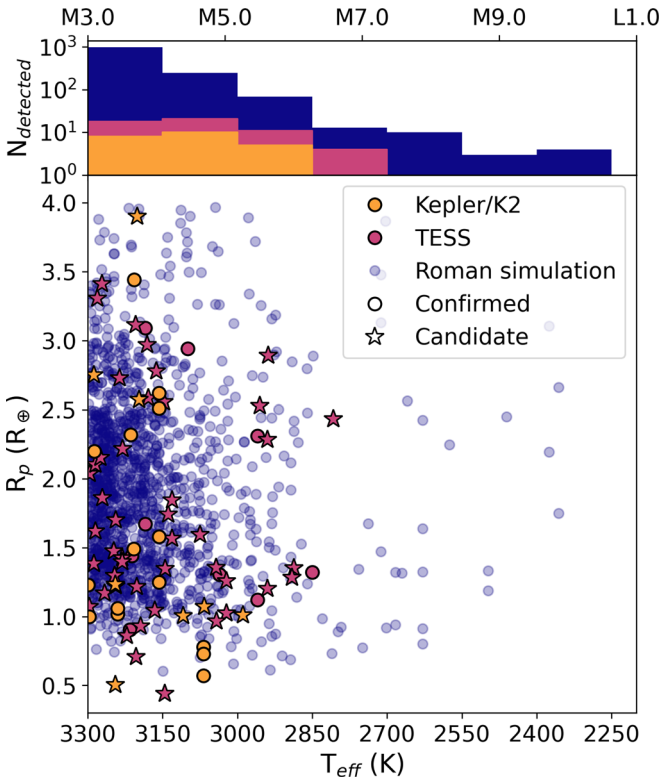

Figure 8. Radii of confirmed (circles) and candidate planets (stars) smaller than 4 $R_\oplus$ vs. effective temperature for hosts with $T_{\rm eff} < 3300$ K from the Kepler/K2 (orange) and TESS (pink) missions. Detections from a representative iteration of our simulation (with 1347 total detections) are shown in blue. The effective temperature is listed on the bottom axis while the approximate spectral types are given along the top axis. The top panel shows histograms of the number of planet detections as a function of effective temperature for the different missions.

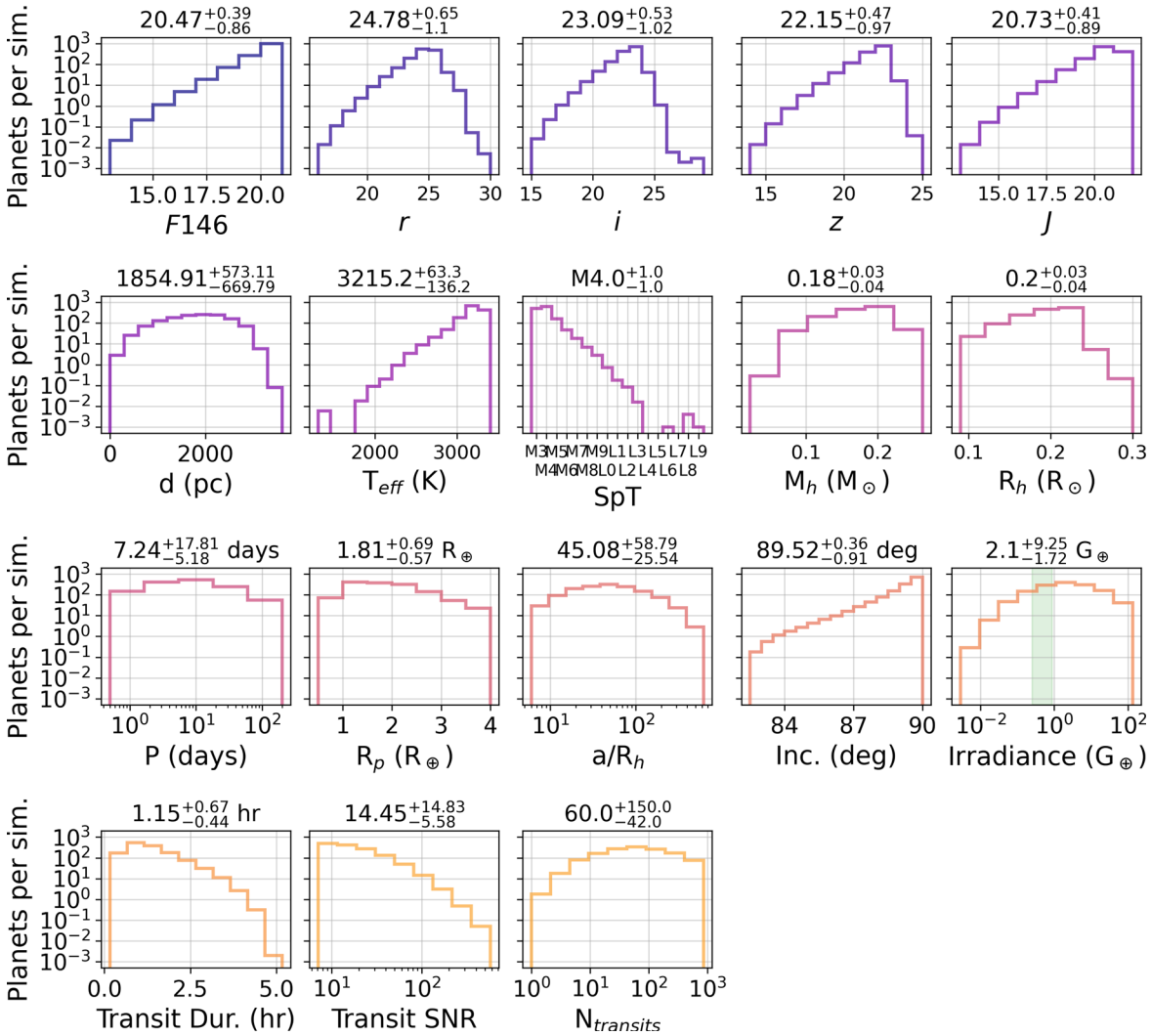

Figure 9. Properties of the transiting planet hosts and transiting planets detected across our 1000 simulations. As in Figure 5, the distributions are shown on a log scale and were normalized to show the average counts in a single simulation. The 15.9%, 50%, and 84.1% percentiles are reported at the top of each panel. First row: F146-, *r*-, *i*-, *z*-, and *J*-band magnitudes of hosts with detected transiting planets. Second row: distance in parsecs, $T_{\rm eff}$ in Kelvin, spectral types, masses in $M_\odot$, and radii in $R_\odot$ of the hosts with detected transiting planets. Third row: orbital periods, radii in $R_\oplus$, a/R_h, inclinations in degrees, and irradiances in Earth irradiance ($G_\oplus$) of the detected transiting planets. The irradiance distribution includes a shaded area indicating the conservative HZ of Kopparapu et al. (2013). Fourth row: durations in hours, S/N, and number of transits of detected transiting planets.

detect a few dozen planets around UCDs, spectral types that have no confirmed or candidate planets from Kepler or TESS.

Very few planets were detected around L- or T-type dwarfs in our simulations, with an average of 1^{+1}_{-1} detection per simulation. We expect that the search for transiting planets around brown dwarfs will remain the purview of dedicated NIR ground-based surveys like SPECULOOS (Delrez et al. 2018; Murray et al. 2020) and PINES (Tamburo et al. 2022a) for the foreseeable future. However, the proposed TEMPO survey of the ONC with Roman will be capable of detecting dozens of planets around brown dwarfs and free-floating planetary-mass objects, because the proximity (∼400 pc) and young ages (∼1–3 Myr) of these sources make them much brighter on average than the sources in the survey (Limbach et al. 2023).

We show the distributions of the detected planet properties in Figure 9. The average planet had an orbital period of $7.2^{+17.8}_{-5.2}$ days, a radius of $1.8^{+0.7}_{-0.6}$ $R_\oplus$, an a/R_h of $45.1^{+58.8}_{-25.5}$, an irradiance of $2.1^{+9.3}_{-1.7}$ $G_\oplus$, a transit duration of $1.2^{+0.7}_{-0.4}$ hr, and was detected to an S/N of $14.5^{+14.8}_{-5.6}$ with an average of 60^{+150}_{-42} transits.

As discussed in Section 3.2, we use the transit S/N of a target's phase-folded light curve to determine whether an injected planet is recovered or not; we impose no constraints on the minimum number of transits for a planet to be considered detected. Our detections therefore include some planets with fewer than three transits, which would require further transit detections to measure their true orbital periods. However, since the maximum orbital periods of our injected planets are 200 days, and since the simulated light curves consist of 432 days of data, such detections are rare. We find just 0.02% of our detected planets exhibit single transits in the light curves, while 0.11% transit twice.

As noted in Section 2.1, our photometric model assumes a constant noise floor of 1 mmag, which becomes the dominant noise source at magnitudes brighter than F146 ≈ 16.8. Only 0.3% of the planets in our simulation were detected around sources with F146 < 16.8, indicating that the assumed noise floor has a negligible impact on the total planet yield.

Finally, as discussed in Section 3.2, a detection threshold of ∼8.1σ may be appropriate for the Roman survey in order to

limit the number of statistical false positive transit detections to one. On average, we find that 91% of our detections have S/N values greater than 8.1, meaning that our total transit yield would be lower by 9% if the more conservative detection threshold was adopted.

4.2. Habitable Terrestrial Transiting Planet Yield

Terrestrial planets around mid-to-late-M dwarfs enable the atmospheric characterization of habitable Earth-sized planets with current and near-future telescope facilities (e.g., Morley et al. 2017). We performed a simple assessment of the habitability of planets in our simulation by calculating the irradiance of each in Earth irradiance:

$$\frac{G}{G_\oplus} = \frac{L}{4\pi a^2 G_\oplus} = \frac{\sigma R_h^2 T_{\rm eff}^4}{a^2 G_\oplus}, \quad (6)$$

where σ is the Stefan–Boltzmann constant, R_h is the radius of the host, $T_{\rm eff}$ is the effective temperature of the host, a is the semimajor axis of the planet's orbit, and $G_\oplus$ is the Earth's average annual irradiance at the top of the atmosphere, which is about 1361 W m^{-2}. We considered a planet to be "habitable" if it experienced an irradiance between 0.25–0.88 $G_\oplus$, the limits of the conservative maximum greenhouse/moist greenhouse habitable zone (HZ) irradiance limits of Kopparapu et al. (2013).

Under the assumed DC15 occurrence rates, we predict an average of 37^{+8}_{-7} habitable planets with radii less than 1.48 $R_\oplus$, the boundary between rocky and nonrocky worlds identified by Rogers (2015). These planets are detected around stars with an average F146 magnitude of $20.1^{+0.6}_{-1.1}$. If we instead assume the smaller rocky/nonrocky planet transition of 1.23 $R_\oplus$ identified by Chen & Kipping (2017), we predict an average of 13^{+4}_{-3} habitable terrestrial planet detections. These planets, being smaller, are preferentially detected around slightly brighter stars, with an average F146 magnitude of $19.9^{+0.8}_{-1.3}$. However, it should be noted that it is difficult to assess whether or not a planet is rocky on the basis of its radius alone due to degeneracies with mass and composition. For example, Unterborn et al. (2023) showed that there exist regions of radius–mass–composition space in which planets are "nominally rocky" up to the 2 $R_\oplus$ limit that was considered in their study.

Regardless, it is exceedingly unlikely that the atmospheres of transiting HZ terrestrial planets detected by Roman around mid-M dwarfs and UCDs will be detectable with JWST. Their host stars will be roughly 10 magnitudes fainter on average than the planet hosts for which these measurements are currently feasible. While a full assessment of the feasibility of atmospheric observations of these planets is beyond the scope of this work, their characterization would likely be infeasible even with the next generation of space telescopes like the Large UV/Optical/Infrared Surveyor (LUVOIR), whose 15 m design (LUVOIR-A) will have a factor of ∼5× the light collecting area of JWST (The LUVOIR Team 2019).

4.3. Yield Differences with Scaled Planet Occurrence Rates

As noted in Section 1, Hardegree-Ullman et al. (2019; hereafter HU19) measured a tentative increase in the occurrence rates of short-period planets with orbital periods between 0.5 and 10 days and radii between 0.5 and 2.5 $R_\oplus$ around mid-type M dwarfs, reporting $0.86^{+1.32}_{-0.68}$, $1.36^{+2.30}_{-1.02}$, and $3.07^{+5.49}_{-2.49}$ such planets per star over the M3, M4, and M5 spectral types, respectively. DC15 measured 0.62 such planets around early-M dwarfs, so the HU19 results suggest a progressive increase in the occurrence rates of such planets out to mid-M spectral types (albeit with large error bars).

We performed a version of our planet injection and recovery simulation with scaled DC15 planet occurrence rates to test whether the Roman time domain survey can reveal the enhancement around mid-M spectral types reported in HU19. Specifically, we again applied the occurrence rate grid of DC15, but scaled their reported occurrence rates for planets with radii between 0.5 and 2.5 $R_\oplus$ and periods between 0.5 and 10 days. We enhanced the occurrence rates around M3 dwarfs by a factor of $0.86/0.62 = 1.39$, around M4 dwarfs by a factor of $1.36/0.62 = 2.19$, and around M5 dwarfs by a factor of $3.07/0.62 = 4.98$. The occurrence rates of planets around later spectral types or outside of the specified radius and period limits were left unchanged.

Figure 10 shows the effect on planet yield for M3–M5 dwarfs, specifically. In the top panel, it shows the distributions of transiting planets with radii 0.5–2.5 $R_\oplus$ and orbital periods between 0.5 and 10 days around M3–M5 dwarfs detected across all 1000 simulations for planet populations with the DC15 and HU19 occurrence rates. The bottom panel shows the cumulative distribution functions of the two distributions. An average of 676^{+105}_{-69} such planets are detected under the assumption of the DC15 occurrence rates, whereas 1411^{+226}_{-133} are detected on average assuming the HU19 occurrence rates. These two average predictions are different by 4.3σ, which suggests that the yield of transiting planets from the Roman survey will be able to determine whether planet occurrence rates are enhanced around mid-M dwarf and UCDs compared to early-M dwarfs to high significance. However, this prediction assumes that the enhanced metallicity expected for our sources (up to [Fe/H] ≈0.3, see Section 2.2.1) does not significantly affect the occurrence rates of short-period planets smaller than 2.5 $R_\oplus$, and this assumption would have to be tested in reality.

5. Conclusions

In this paper, we investigated the potential of the Nancy Grace Roman Space Telescope time domain survey of the Galactic bulge for the purposes of detecting transiting exoplanets around mid-M dwarfs and UCDs.

We summarize our results as follows:

1. We predict an average of $75{,}500^{+11{,}800}_{-7000}$ single mid-M dwarfs and UCDs in the Roman time domain survey fields with F146 < 21, a quantity that lies between the predictions from two stellar population synthesis codes, `Besançon` and `TRILEGAL`.
2. We predict an average of 1347^{+208}_{-124} transiting planet detections around single mid-M dwarf and UCD sources in the Roman survey if their planet population matches that measured for early-M dwarfs in DC15. This quantity of detections will permit constraints on planet occurrence rates out to spectral type ∼M7.
3. A couple dozen planets will be detected around spectral types M7–M9, but few (if any) will be detected around L- and T-type dwarfs. The detection of transiting planets around brown dwarfs will thus likely remain the purview of dedicated ground-based surveys like SPECULOOS (Delrez et al. 2018; Murray et al. 2020) and PINES (Tamburo et al.

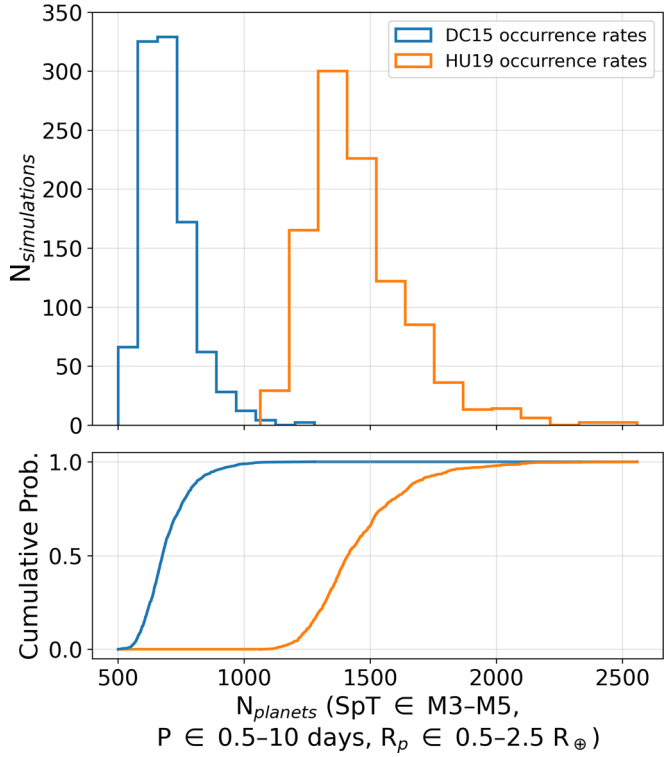

Figure 10. Top: distributions of detected planets with radii between 0.5 and 2.5 $R_\oplus$ and orbital periods between 0.5 and 10 days around M3–M5 dwarfs in our simulations. The results using the DC15 planet occurrence rates for early-M dwarfs are shown in blue, and the results using the HU19 enhanced planet occurrence rates for M3–M5 dwarfs are shown in orange. Bottom: cumulative distribution functions for the two distributions shown in the top panel.

2022a), though the proposed TEMPO survey of the ONC with Roman (Limbach et al. 2023) will be able to detect dozens of planets around young brown dwarfs. The Rubin LSST project may also be capable of probing this parameter space with its Deep Drilling Fields (e.g., Lund et al. 2015; Ivezić et al. 2019), but will be subject to the normal limitations of ground-based observations for making transiting exoplanet discoveries.

4. We predict the detection of 37^{+8}_{-7} planets within the conservative Kopparapu et al. (2013) HZ with radii smaller than 1.48 $R_\oplus$, and 13^{+4}_{-3} with radii smaller than 1.23 $R_\oplus$. These radius limits correspond to the transitions between rocky and gaseous planets identified in Rogers (2015) and Chen & Kipping (2017), respectively. However, except in rare cases, we predict that the atmospheres of these planets will not be characterizable with current or near-future space telescope facilities, owing to the faintness of their host stars.
5. If the occurrence rates of planets smaller than 2.5 $R_\oplus$ on orbital periods less than 10 days are enhanced around M3–M5 dwarfs as measured in HU19, the yield of transiting planets from the survey could reveal that enhancement to a significance of over 4σ. However, we note that the Roman survey will detect planets around stars with slightly higher average metallicities than the early-M dwarf hosts that were observed with Kepler, so the effects of metallicity will have to be accounted for when determining the significance of an observed enhancement in the planet occurrence rates.

Our conclusions are subject to several important caveats which should be borne in mind when interpreting our results. For one, we simulated light curves assuming purely Gaussian noise, neglecting effects from systematics (e.g., intrapixel effects) or source variability (e.g., rotation or flares). Contributions from these noise sources would only serve to decrease our expected planet yield. Second, we have ignored the fact that the planet occurrence rates for early-M dwarfs can be better explained by a dual-population mixture model rather than the single population that we have assumed here (Ballard & Johnson 2016). Our results, therefore, likely underestimate the number of single-planet systems and overestimate the number of two-planet systems, and potentially underestimate the total transiting planet yield compared to multiple-population models (e.g., Ballard 2019). Third, we have implicitly assumed that all transiting planets that are detectable to a significance of at least 7.1σ in the survey data *will* be detected, and we did not consider statistical or astrophysical false positives. Confirming the planetary nature of all candidate systems found in the survey data will require significant effort and will be complicated by the crowded nature of the survey fields, which will have a crowding rate about two times higher than Kepler (Montet et al. 2017). In a related manner, we did not consider the effects of flux contamination in our simulations, which would serve to reduce the S/N of transit events and reduce the total planet yield. Finally, we performed our planet injection and recovery simulation assuming the "Cycle 7" design of the Roman survey as described in Penny et al. (2019). The exact implementations of Roman's three Core Community Surveys have not yet been finalized, and changes to the design of the survey (e.g., number of fields, cadence, filter choices, etc.) would naturally affect our predicted planet yield.

With these caveats in mind, our results have demonstrated that the Nancy Grace Roman Space Telescope survey has the potential to transform our understanding of the planet occurrence rates around very-low-mass stars, optically faint sources that have not yet been probed with sufficiently sensitive data in a large-scale transit survey. These constraints are needed to differentiate between two competing predictions: occurrence rate trends from the Kepler mission, which found a significant anticorrelation between host mass and the occurrence rate of short-period 1–4 $R_\oplus$ transiting exoplanets, and planet formation models, which generally predict that the formation of super-Earths and mini-Neptunes should become more difficult around mid-M dwarfs and later. Data from the Roman survey will be sensitive enough to place these constraints on spectral types out to ∼M7, and will vastly improve our understanding of planetary systems around objects at the bottom of the main sequence. Based on the stellar IMF, mid-M dwarfs and UCDs are some of the most common outcomes of the star formation process; as a result, their planets may comprise the bulk of the galactic census of exoplanets. Roman represents the first mission with the capacity to test this possibility and it could allow us to understand our own solar system in a galactic context for the first time.

The authors thank their anonymous referee, whose comments improved the quality of this work.

This material is based upon work supported by the National Aeronautics and Space Administration under grant No. 80NSSC20K0256 issued through the Science Mission Directorate.

This research has made use of the NASA Exoplanet Archive, which is operated by the California Institute of Technology, under contract with the National Aeronautics and Space Administration under the Exoplanet Exploration Program.

The authors thank Jennifer Winters for helpful input regarding the binarity of sources in the W21 sample.

Facility: NASA Exoplanet Archive.

Software: `BATMAN` (Kreidberg 2015), `Besançon` (Robin et al. 2003), `dustmaps` (Green 2018), `Forecaster` (Chen & Kipping 2017), and `TRILEGAL` (Girardi et al. 2005).

ORCID iDs

Patrick Tamburo https://orcid.org/0000-0003-2171-5083
Philip S. Muirhead https://orcid.org/0000-0002-0638-8822
Courtney D. Dressing https://orcid.org/0000-0001-8189-0233

References

Ahmed, S., & Warren, S. J. 2019, A&A, 623, A127
Akeson, R., Armus, L., Bachelet, E., et al. 2019, arXiv:1902.05569
Allard, F., Homeier, D., & Freytag, B. 2012, RSPTA, 370, 2765
Anderson, S. G., Dittmann, J. A., Ballard, S., & Bedell, M. 2021, AJ, 161, 203
Andrews, S. M., Rosenfeld, K. A., Kraus, A. L., & Wilner, D. J. 2013, ApJ, 771, 129
Andrievsky, S. M., Bersier, D., Kovtyukh, V. V., et al. 2002, A&A, 384, 140
Arenou, F. 2011, in AIP Conf. Ser. 1346, Int Workshop on Double and Multiple Stars: Dynamics, Physics, and Instrumentation, ed. J. A. Docobo, V. S. Tamazian, & Y. Y. Balega (Melville, NY: AIP), 107
Ballard, S. 2019, AJ, 157, 113
Ballard, S., & Johnson, J. A. 2016, ApJ, 816, 66
Baraffe, I., Homeier, D., Allard, F., & Chabrier, G. 2015, A&A, 577, A42
Bashi, D., Helled, R., Zucker, S., & Mordasini, C. 2017, A&A, 604, A83
Bastian, N., Covey, K. R., & Meyer, M. R. 2010, ARA&A, 48, 339
Bessell, M. S. 2005, ARA&A, 43, 293
Bland-Hawthorn, J., & Gerhard, O. 2016, ARA&A, 54, 529
Bonfils, X., Delfosse, X., Udry, S., et al. 2005, A&A, 442, 635
Borucki, W. J., Koch, D., Basri, G., et al. 2010, Sci, 327, 977
Bouma, L. G., Masuda, K., & Winn, J. N. 2018, AJ, 155, 244
Brady, M. T., & Bean, J. L. 2022, AJ, 163, 255
Chabrier, G. 2001, ApJ, 554, 1274
Chabrier, G. 2003, PASP, 115, 763
Chambers, K. C., Magnier, E. A., Metcalfe, N., et al. 2016, arXiv:1612.05560
Chen, J., & Kipping, D. 2017, ApJ, 834, 17
Churchwell, E., Babler, B. L., Meade, M. R., et al. 2009, PASP, 121, 213
Claret, A., & Bloemen, S. 2011, A&A, 529, A75
Czekaj, M. A., Robin, A. C., Figueras, F., Luri, X., & Haywood, M. 2014, A&A, 564, A102
Delfosse, X., Forveille, T., Ségransan, D., et al. 2000, A&A, 364, 217
Delrez, L., Gillon, M., Queloz, D., et al. 2018, Proc. SPIE, 10700, 107001I
Domber, J. L., Gygax, J. D., Aumiller, P., et al. 2022, Proc. SPIE, 12180, 121801O
Domber, J. L., Wilkinson, E., Nicks, D., Delker, T., & Lipscy, S. J. 2019, Proc. SPIE, 11115, 1111502
Dressing, C. D., & Charbonneau, D. 2013, ApJ, 767, 95
Dressing, C. D., & Charbonneau, D. 2015, ApJ, 807, 45
Fabrycky, D. C., Lissauer, J. J., Ragozzine, D., et al. 2014, ApJ, 790, 146
Faherty, J. K., Riedel, A. R., Cruz, K. L., et al. 2016, ApJS, 225, 10
Fischer, D. A., & Valenti, J. 2005, ApJ, 622, 1102
Gaidos, E., Mann, A. W., Kraus, A. L., & Ireland, M. 2016, MNRAS, 457, 2877
Gaudi, B. S. 2012, ARA&A, 50, 411
Genovali, K., Lemasle, B., Bono, G., et al. 2014, A&A, 566, A37
Gibbs, A., Bixel, A., Rackham, B. V., et al. 2020, AJ, 159, 169
Gillon, M., Jehin, E., Fumel, A., Magain, P., & Queloz, D. 2013, EPJ Web Conf., 47, 03001
Gillon, M., Jehin, E., Lederer, S. M., et al. 2016, Natur, 533, 221
Gillon, M., Triaud, A. H. M. J., Demory, B.-O., et al. 2017, Natur, 542, 456
Girardi, L., Groenewegen, M. A. T., Hatziminaoglou, E., & da Costa, L. 2005, A&A, 436, 895
Green, G. M. 2018, JOSS, 3, 695
Green, G. M., Schlafly, E., Zucker, C., Speagle, J. S., & Finkbeiner, D. 2019, ApJ, 887, 93
Green, G. M., Schlafly, E. F., Finkbeiner, D., et al. 2018, MNRAS, 478, 651
Green, G. M., Schlafly, E. F., Finkbeiner, D. P., et al. 2015, ApJ, 810, 25
Gaia Collaboration, Prusti, T., de Bruijne, J. H. J., et al. 2016, A&A, 595, A1
Hardegree-Ullman, K. K., Cushing, M. C., Muirhead, P. S., & Christiansen, J. L. 2019, AJ, 158, 75
He, M. Y., Triaud, A. H. M. J., & Gillon, M. 2017, MNRAS, 464, 2687
Hippke, M., & Heller, R. 2019, A&A, 623, A39
Hodgkin, S. T., Harrison, D. L., Breedt, E., et al. 2021, A&A, 652, A76
Howard, A. W., Marcy, G. W., Bryson, S. T., et al. 2012, ApJS, 201, 15
Ivezić, Ž., Kahn, S. M., Tyson, J. A., et al. 2019, ApJ, 873, 111
Jenkins, J. M., Caldwell, D. A., & Borucki, W. J. 2002, ApJ, 564, 495
Johnson, J. A., Aller, K. M., Howard, A. W., & Crepp, J. R. 2010, PASP, 122, 905
Johnson, S. A., Penny, M., Gaudi, B. S., et al. 2020, AJ, 160, 123
Kirkpatrick, J. D., Gelino, C. R., Faherty, J. K., et al. 2021, ApJS, 253, 7
Kirkpatrick, J. D., Henry, T. J., & Irwin, M. J. 1997, AJ, 113, 1421
Kopparapu, R. K., Ramirez, R., Kasting, J. F., et al. 2013, ApJ, 765, 131
Kovács, G., Zucker, S., & Mazeh, T. 2002, A&A, 391, 369
Kreidberg, L. 2015, PASP, 127, 1161
Kroupa, P. 2002, Sci, 295, 82
Lienhard, F., Queloz, D., Gillon, M., et al. 2020, MNRAS, 497, 3790
Limbach, M. A., Soares-Furtado, M., Vanderburg, A., et al. 2023, PASP, 135, 014401
Limbach, M. A., Vos, J. M., Winn, J. N., et al. 2021, ApJL, 918, L25
Lund, M. B., Pepper, J., & Stassun, K. G. 2015, AJ, 149, 16
Mann, A. W., Dupuy, T., Kraus, A. L., et al. 2019, ApJ, 871, 63
Mann, A. W., Feiden, G. A., Gaidos, E., Boyajian, T., & von Braun, K. 2015, ApJ, 804, 64
Mann, A. W., Gaidos, E., Kraus, A., & Hilton, E. J. 2013, ApJ, 770, 43
Marley, M. S., Saumon, D., Visscher, C., et al. 2021, ApJ, 920, 85
McMillan, P. J. 2017, MNRAS, 465, 76
Mennesson, B., Juanola-Parramon, R., Nemati, B., et al. 2020, arXiv:2008.05624
Ment, K., & Charbonneau, D. 2023, arXiv:2302.04242
Montet, B. T., Yee, J. C., & Penny, M. T. 2017, PASP, 129, 044401
Morley, C. V., Kreidberg, L., Rustamkulov, Z., Robinson, T., & Fortney, J. J. 2017, ApJ, 850, 121
Mulders, G. D., Drazkowkska, J., van der Marel, N., Ciesla, F. J., & Pascucci, I. 2021, ApJL, 920, L1
Mulders, G. D., Pascucci, I., & Apai, D. 2015, ApJ, 798, 112
Murray, C. A., Delrez, L., Pedersen, P. P., et al. 2020, MNRAS, 495, 2446
Ning, B., Wolfgang, A., & Ghosh, S. 2018, ApJ, 869, 5
Noecker, M. C., Zhao, F., Demers, R., et al. 2016, JATIS, 2, 011001
Pascucci, I., Testi, L., Herczeg, G. J., et al. 2016, ApJ, 831, 125
Pedicelli, S., Bono, G., Lemasle, B., et al. 2009, A&A, 504, 81
Penny, M. T., Gaudi, B. S., Kerins, E., et al. 2019, ApJS, 241, 3
Pinamonti, M., Sozzetti, A., Maldonado, J., et al. 2022, A&A, 664, A65
Pont, F., Zucker, S., & Queloz, D. 2006, MNRAS, 373, 231
Rajpurohit, A. S., Reylé, C., Allard, F., et al. 2013, A&A, 556, A15
Reylé, C., & Robin, A. C. 2001, A&A, 373, 886
Ricker, G. R., Winn, J. N., Vanderspek, R., et al. 2015, JATIS, 1, 014003
Robin, A. C., Marshall, D. J., Schultheis, M., & Reylé, C. 2012, A&A, 538, A106
Robin, A. C., Reylé, C., Derrière, S., & Picaud, S. 2003, A&A, 409, 523
Rogers, L. A. 2015, ApJ, 801, 41
Sabotta, S., Schlecker, M., Chaturvedi, P., et al. 2021, A&A, 653, A114
Sagear, S. A., Skinner, J. N., & Muirhead, P. S. 2020, AJ, 160, 19
Santos, N. C., Israelian, G., & Mayor, M. 2004, A&A, 415, 1153
Schlafly, E. F., Green, G. M., Lang, D., et al. 2018, ApJS, 234, 39
Sebastian, D., Gillon, M., Ducrot, E., et al. 2021, A&A, 645, A100
Sestovic, M., & Demory, B.-O. 2020, A&A, 641, A170
Skrutskie, M. F., Cutri, R. M., Stiening, R., et al. 2006, AJ, 131, 1163
Spergel, D., Gehrels, N., Baltay, C., et al. 2015, arXiv:1503.03757
Tamburo, P., Muirhead, P. S., McCarthy, A. M., et al. 2022a, AJ, 163, 253
Tamburo, P., Muirhead, P. S., McCarthy, A. M., et al. 2022b, AJ, 164, 252
The LUVOIR Team 2019, arXiv:1912.06219
Ulmer-Moll, S., Santos, N. C., Figueira, P., Brinchmann, J., & Faria, J. P. 2019, A&A, 630, A135
Unterborn, C. T., Desch, S. J., Haldemann, J., et al. 2023, ApJ, 944, 42
Weiss, L. M., Marcy, G. W., Rowe, J. F., et al. 2013, ApJ, 768, 14
Winters, J. G., Charbonneau, D., Henry, T. J., et al. 2021, AJ, 161, 63
Wolfgang, A., Rogers, L. A., & Ford, E. B. 2016, ApJ, 825, 19
Wright, E. L., Eisenhardt, P. R. M., Mainzer, A. K., et al. 2010, AJ, 140, 1868